Southern Ocean heat uptake, redistribution and storage in a warming climate: The role of meridional overturning circulation

Wei Liu*

Department of Earth Sciences, University of California Riverside, Riverside, CA, USA

Scripps Institute of Oceanography, University of California San Diego, La Jolla, CA, USA

Department of Geology and Geophysics, Yale University, New Haven, CT, USA

Jian Lu

Pacific Northwest National Laboratory, Richland, WA, USA

Shang-Ping Xie

Scripps Institute of Oceanography, University of California San Diego, La Jolla, CA, USA

Alexey Fedorov

Department of Geology and Geophysics, Yale University, New Haven, CT, USA

**Corresponding author address:* Geology Building, 900 University Ave., Riverside, CA, 92521

E-mail: wei.liu@ucr.edu

ABSTRACT

Climate models show that most of the anthropogenic heat due to increased atmospheric CO_2 enters the Southern Ocean near 60^{o}S and is stored around 45^{o}S. This heat is transported to the ocean interior by the meridional overturning circulation (MOC) with wind changes playing an important role in the process. To isolate and quantify the latter effect, we apply an overriding technique to a climate model and decompose the total ocean response to CO_2 increase into two major components: one due to wind changes and the other due to direct CO_2 effect. We find that the poleward-intensified zonal surface winds tend to shift and strengthen the ocean Deacon Cell and hence the residual MOC, leading to anomalous divergence of ocean meridional heat transport around 60^{o}S coupled to a surface heat flux increase. In contrast, at 45^{o}S we see anomalous convergence of ocean heat transport and heat loss at the surface. As a result, the wind-induced ocean heat storage (OHS) peaks at 46^{o}S at a rate of 0.07 ZJ/year (1ZJ = 10^{21} joules) in unit degree of latitude, contributing 20% to the total OHS maximum. The direct CO_2 effect, on the other hand, very slightly alters the residual MOC but primarily warms the ocean. It induces a small but non-negligible change in eddy heat transport and causes OHS to peak at 42^{o}S at a rate of 0.30 ZJ/year in unit latitudinal degree that accounts for 80% of the OHS maximum. We also find that the eddy-induced MOC weakens, which is primarily caused by a buoyancy flux change due to the direct CO_2 effect, and does not compensate the intensified Deacon Cell.

1. Introduction

Observations reveal a pronounced subsurface warming in the Southern Ocean during the past few decades [e.g., Gille (2002); Purkey and Johnson (2010); Durack et al. (2014); Roemmich et al. (2015)]. This subsurface warming and increased ocean heat content (OHC) correspond to enhanced ocean heat uptake [Frölicher et al. (2015); Roemmich et al. (2015)] and cause the observed sea level rise over the Southern Ocean [Church et al. (2011); Church et al. (2013)]. In general, the Southern Ocean heat uptake is important for regional sea level change [van der Veen (1988); Gregory et al. (2001)], delayed sea surface temperature response [Bryan et al. (1988); Manabe et al. (1991); Armour et al. (2016)], transient climate sensitivity and related feedbacks [Winton et al. (2010); Rose et al. (2014)], and understanding the recent global surface warming hiatus [Liu et al. (2016); Chen and Tung (2014)]. A recent study also suggested remote effects of the enhanced heat uptake over the Southern Ocean on tropical rainfall and monsoons (Hwang et al. 2017).

An early modeling study of Manabe et al. (1990) suggested that the Southern Ocean takes up heat in global warming via a reduction in convective ocean heat loss. Gregory (2000) further found that the weakened convection acts to reduce the entrainment of heat into the mixed layer from below and finally leads to a decline in upward diffusion of heat along isopycnals below the mixed layer [also see Huang et al. (2003)]. In the Southern Ocean interior, the balance is maintained between northward/downward heat transport by the mean flow and southward/upward heat transport by eddies (Gregory 2000). In a warming climate, the heat balance changes, modifying ocean heat uptake and heat distribution [e.g., Griffies et al. (2015)]. Two primary processes have been proposed for the heat balance change: decrease in southward/upward eddy heat transport [Gregory (2000); Dalan et al. (2005); Hieronymus and Nycander (2013); Morrison et al. (2013)], or increase in northward/downward advective heat transport by the time mean flow [Cai et al. (2010); Kuhlbrodt and Gregory (2012); Marshall and Zanna (2014); Bryan et al. (2014); Exarchou et al. (2015)]. Recently, Morrison et al. (2016) found that both processes could be important. The mean flow and eddy processes dominate, respectively, to the south and north of the main convergence region.

Marshall et al. (2015) simulated a mute Southern Ocean surface warming using an ocean general circulation model forced with a spatially uniform surface flux. But to what extent does the heat taken from the atmosphere and distributed into the ocean interior behave like a passive tracer advected along the mean ventilation pathways? Using a passive tracer technique, Banks and Gregory (2006) concluded that the interior temperature change in the Southern Ocean cannot be explained solely by passive tracer transport along isopycnals, since ocean circulation changes also affect heat distribution [see also Xie and Vallis (2012)]. Winton et al. (2013) explored this question from a different perspective. Holding ocean circulation fixed, they found that modifying ocean circulation can effectively redistribute heat over the Southern Ocean, which was generally consistent with the results of Banks and Gregory (2006). Both Banks and Gregory (2006) and Winton et al. (2013) discussed the role of ocean circulation changes in Southern Ocean heat uptake and redistribution.

Under anthropogenic forcing, the Southern Ocean circulation is suggested to be primarily affected by surface wind stress changes [e.g., Gillett and Thompson (2003); Fyfe (2006)] [note here, changes in surface bouyancy forcing also play a role, c.f., Sen Gupta et al. (2009)]. Particularly, observations show a poleward shift and strengthening of Southern Hemisphere westerly winds (Swart and Fyfe 2012) due to ozone depletion [e.g., Gillett and Thompson (2003)] and increasing greenhouse gases [e.g., Fyfe (2006)], with the Southern Annual Mode (Marshall 2003) shifting toward a higher index state (Thompson and Solomon 2002). The poleward intensified winds strengthen and displace the Eulerian-mean meridional overturning circulation (MOC), of-ten referred to as the Deacon Cell [e.g., Sen Gupta and England (2006); Sen Gupta et al. (2009); Downes and Hogg (2013)], although this wind-driven circulation change has been suggested to be partially compensated by an increased eddy activity due to enhanced baroclinicity [e.g., Hallberg and Gnanadesikan (2006); Hogg et al. (2008); Farneti et al. (2010); Wolfe and Cessi (2010); Abernathey et al. (2011); Bishop et al. (2016)].

To isolate the effects of wind change on the Southern Ocean MOC and heat uptake, and hence temperature and heat storage in a warming climate, several studies [e.g., Oke and England (2004); Fyfe et al. (2007); Spence et al. (2010)] perturbed surface wind stress alone using a wind pattern derived from global warming experiments. They found that poleward-intensified winds cause a subsurface warming around 45^{o}S via an increased downwelling of warm surface water, and a cooling at higher and lower latitudes. Although these studies confirmed the wind effect on heat uptake and redistribution in the Southern Ocean, they could not rigorously quantify this effect by means of a consistent heat budget analysis as they used either forced ocean general circulation models (Oke and England 2004) or ocean models coupled to an energy-balance model of the atmosphere [Fyfe et al. (2007); Spence et al. (2010)]. Therefore, the ocean-atmosphere coupling was missing or distorted. For example, wind-induced changes in sea surface temperature (SST) and surface heat flux will feed back on the atmospheric storm tracks, precipitation and clouds. It is essential to consider such feedbacks when examining ocean heat uptake.

In this study, we employ an overriding technique [Lu and Zhao (2012); Liu et al. (2015)] to isolate and quantify the effects of wind change and related feedbacks on Southern Ocean heat uptake and redistribution. For example, we override surface winds in a fully coupled system from a quadrupled CO_2 climate and separate the wind-induced feedback from other feedbacks in term of contributions to the total climate response. Unlike previous studies, our overriding method can practically disable the wind change effect while allowing other atmospheric processes to be fully interactive with the ocean. This allows us to estimate the wind-induced feedback along with the direct CO_2 effect and quantify its contribution to the Southern Ocean heat uptake and redistribution through a consistent heat budget analysis.

The structure of the paper is as follows. In Section 2, we introduce the models, experiments and metrics used in this study, with a particular emphasis on the overriding technique. We present the main results in Section 3, and the paper's conclusion and discussion in Section 4.

2. Methods

a. CMIP5 models and simulations

To study the characteristics of Southern Ocean heat uptake and redistribution to increasing CO_2, we analyze the pre-industrial control (*piControl*) and abruptly quadrupled CO_2 ($abrupt4 \times CO_2$) simulations of ten climate models (Table 1) participating in the Coupled Model Intercomparison Project Phase 5 [CMIP5, Taylor et al. (2012)]. The abruptly quadrupled CO_2 represents an idealized global warming scenario in which the atmospheric concentration of CO_2 is instantaneously quadrupled from its initial preindustrial value and then held fixed. We examine the changes of several variables (Table 1) that are related to Southern Ocean heat uptake and redistribution. For each variable, the change is defined as the differences between years 41-90 after CO_2, quadrupling and a 50-year average in *piControl*. Note here, our analysis of year 41-90 change is an investigation of transient climate response to CO_2 increase, since the abyssal ocean will need thousands of years to reach equilibrium after quadrupled CO_2. It also merits attention that the Southern Ocean SST and therefore heat uptake and storage show a fast (over years) and slow (over decades) response to a given forcing [Ferreira et al. (2015); Kostov et al. (2017)], whereas our choice of year 41-90 change does not account for the fast response.

In our analysis, most variables are available across the ten models (Table 1). For the eddy-induced MOC and meridional ocean heat transport, both of them are only available in ACCESS1-0, ACCESS1-3 and CCSM4. Thus we just use these three models for MOC and heat transport analyses. Besides, we only analyze the first member run (r1i1p1) of each model to ensure equal weight in inter-model analysis.

b. CESM and overriding experiments

We use the Community Earth System Model (CESM) (Hurrell et al. 2013), version 1.0.5 from the National Center for Atmospheric Research (NCAR) that includes the latest version of the Community Atmosphere Model version 5 [CAM5, e.g., Neale and coauthors (2012)], the Community Land Model version 4 [CLM4, Lawrence et al. (2012)], the sea ice component version 4 [CICE4, Holland et al. (2012)] and the Parallel Ocean Program version 2 [POP2, Smith and coauthors (2010)], and henceforth is called CESM1-CAM5. The f19gx1v6 version used here has a finite-volume dynamical core (Lin 2004) with a nominal 2^{o} atmosphere and land horizontal grid ($1.9^{\text{o}}\times 2.5^{\text{o}}$ latitude versus longitude) with 26 atmospheric layers in the vertical, and a nominal 1^{o} ocean and ice horizontal grid (referred to as x1) with 60 ocean layers in the vertical. Over the Southern Ocean, the meridional resolution of POP2 is about 0.5^{o}. Although the ocean model is not eddy-resolved, it employs a variable coefficient in the Gent-McWilliams eddy parameterization [Gent and Mcwilliams (1990), hereafter GM], which enables an appropriate ocean response to wind change as indicated eddy-resolving models (Gent and Danabasoglu 2011). For tracers, such as temperature, the horizontal diffusion follows the Redi isoneutral diffusion operator by the GM parameterization and the vertical diffusion (mixing) follows the K-profile parameterization [KPP, c.f. Large et al. (1994)].

The baseline runs of this study are a preindustrial control run (*CTRL*) and a quadruple CO_2 run ($4 \times CO_2$), which are identical to the *piControl* and *abrupt* $4 \times CO_2$ simulations by CMIP5 models. Here, we rename these two CESM runs for the convenience of discussion. *CTRL* is taken from the NCAR CESM-CAM5 f19gx1v6 simulation in the preindustrial 1850 A.D. scenario and the $4 \times CO_2$ branches from the *CTRL*, with the atmospheric CO_2 concentration instantly quadrupled from the 1850 level and kept constant through the 90-year simulation.

In contrast to previous wind perturbation experiments, we employ a partial coupling based on the so-called overriding technique [Lu and Zhao (2012); Liu et al. (2015)] in order to isolate and quantify the contributions of various feedbacks and processes to the Southern Ocean heat uptake and redistribution. The partially coupled CESM1-CAM5 is realized through overriding the time series of one or more variables at the air-sea interface from a fully coupled run to disable the targeted process or feedback. Specifically, it is implemented in the following steps. Let us denote the coupled baseline runs as $c1x$ for *CTRL* and as $c4x$ for $4 \times CO_2$, and the overriding variables from these two runs are first output for overriding purpose at the frequency of air-sea coupling (daily for the case of CESM1-CAM5) and will be referred to respectively as $var1x$ and $var4x$, in which *var* is the overriding variable. In the paper, we consider three variables: wind stress (τ), wind speed (w) and CO_2 (c) because winds can affect surface heat uptake and interior ocean heat distribution either by changing ocean circulation via surface wind stress or by modifying ocean-atmosphere thermal coupling through the wind speed in the bulk formula of turbulent (latent and sensible) heat fluxes. Next, we conduct a suite of overriding experiments (Table 2) to isolate the effect of the variable we are interested in. For example, to target climate response without wind feedback, we run the $4 \times CO_2$ experiment again but with wind stress and wind speed prescribed from *CTRL*. We name this overriding run $\tau 1 w 1 c 4$, denoting wind stress and wind speed from $c1x$ but CO_2 level from $c4x$.

Inevitably, overriding interferes with the temporal coherence between the overriding variable and the processes it interacts with, leading to a climate drift. For instance, if we were overriding the surface wind in $c1x$ case by prescribing $\tau 1x$ and $w1x$ (but shifted by 1 year intentionally), the resultant climate (labeled as $\tau 1w1c1$) would not be the same as that of $c1x$, the difference between them being the drift due to overriding wind stress and wind speed (denoted by $\tau 1w1c1 - CTRL$). Here, the 1-year (or any integer number of years) shift in the time of $\tau 1x$ is intended to disrupt its coherence with other fields in the $c1x$ run; an overriding of $\tau 1x$ without the time shift would be simply a replication of $c1x$. This drift must be identified and excluded in the attribution of the relevant feedbacks, which can be achieved by comparing the overriding runs because the same overriding-induced drift is present in all such runs and the difference between any two of them should eliminate the drift. For example, the direct CO_2 effect in quadrupled CO_2 climate change simulations should be isolated through the operation $(\tau 1w1c4 - CTRL) - (\tau 1w1c1 - CTRL)$, which is the same as $\tau 1w1c4 - \tau 1w1c1$. Therefore, the climate drifts, which should not be one part of the response, are eliminated by the cancellation of drifts in both $\tau 1w1c4 - CTRL$ and $\tau 1w1c1 - CTRL$. As a result, this allows a more accurate estimate of surface heat flux and interior ocean heat distribution.

In summary, the overriding technique enables a linear decomposition of the total response to CO_2 quadrupling in the fully coupled model into the parts due to: (I) surface wind stress change ($\tau 4w1c4 - \tau 1w1c4$); (II) surface wind speed change ($\tau 1w4c4 - \tau 1w1c4$), and (III) the direct CO_2 effect without wind changes ($\tau 1w1c4 - \tau 1w1c1$). As will be shown in later sections, the surface wind speed change (part II) has a minimal effect on Southern Ocean heat uptake and redistribution.

c. MOC

The Eulerian-mean *MOC* is calculated by integrating meridional velocity v zonally and vertically:

$$\overline{\psi}(y,z) = \oint \int_z^0 v \, dz' \, dx \tag{1}$$

where x, y and z are the zonal, meridional and vertical coordinates. This representation of the MOC is largely made up of the wind-driven Ekman circulation known as the Deacon Cell (Döös and Webb 1994). Similarly, the eddy-induced MOC is calculated as

$$\overset{*}{\psi}(y,z) = \oint \int_z^0 v^* dz' \, dx \tag{2}$$

where v^* is eddy-induced velocity. In POP2 ocean model, it is in form of a bolus velocity derived from the GM parameterization. In the Southern Ocean, there is a partial compensation between Eulerian-mean and eddy-induced MOCs [e.g., Marshall and Radko (2003)], yielding a residual MOC (ψ_{res}) as

$$\psi_{res} = \overline{\psi} + \psi^* \tag{3}$$

d. Oceanic heat budget

The zonally integrated full-depth oceanic heat budget is

$$\oint \int_{-H}^0 \rho_0 C_p \frac{\partial \theta}{\partial t} dz' \, dx + \oint \int_{-H}^0 \rho_0 C_p \left[\nabla \cdot (\mathbf{v}\theta + D)\right] dz' \, dx = \oint (SHF) \, dx \tag{4}$$

where ρ_0 is seawater density, C_p is the specific heat of sea water, θ is potential temperature of sea water, $-H$ denotes the depth of ocean bottom. SHF denotes net surface heat flux, which is the sum of radiative shortwave (SW) and longwave (LW) fluxes and turbulent sensible (SH) and latent (LH) heat fluxes. ∇ and $\mathbf{v}$ are three-dimensional gradient operator and velocity, and $\mathbf{v} = \overline{\mathbf{v}} + \mathbf{v}^*$. D denotes diffusion and other sub-grid processes.

Based on Eq. (4), we define the rate of integrated OHC as ocean heat storage, i.e.,

$$OHS = \frac{\partial}{\partial t} \oint \int_{-H}^{0} \rho_0 C_p \, \theta \, dz' \, dx \tag{5}$$

and ocean heat uptake as

$$OHU = \oint (SHF) \, dx \tag{6}$$

and meridional ocean heat transport as

$$OHT = \oint \int_{-H}^{0} \rho_0 C_p \, (\overline{\mathbf{v}}\theta + \mathbf{v}^* \theta + D) \, dz' \, dx = \overline{OHT} + OHT^* + OHT^d \tag{7}$$

where $\overline{OHT} = \oint \int_{-H}^{0} \rho_0 C_p \overline{\mathbf{v}} \theta dz' \, dx$, $OHT^* = \oint \int_{-H}^{0} \rho_0 C_p \mathbf{v}^* \theta dz' \, dx$ and $OHT^d = \oint \int_{-H}^{0} \rho_0 C_p D dz' \, dx$. Eq. (7) shows that meridional ocean heat transport (OHT) can be induced by Eulerian-mean flow ($\overline{OHT}$), eddies (OHT^*) and diffusion (OHT^d). Therefore, the heat budget by Eq. (4) can be written as

$$OHS = OHU - \frac{\partial}{\partial y} OHT \tag{8}$$

which indicates that ocean heat storage is determined by heat uptake from atmosphere-ocean interface and heat retribution by ocean circulation via meridional gradient of ocean heat transport.

3. Results

a. Climate response in CMIP5 models

We first examine the change of SHF and OHU over the Southern Ocean in response to quadrupled CO_2 in CMIP5 models. We find that most heat enters the Southern Ocean over and slightly to the south of the region of the Antarctic Circumpolar Current (ACC) as the deep upwelled water keeps the surface ocean from warming. Particularly, anomalous heat enters (leaves) ocean in zonal bands along the southern (northern) flank of the ACC (Fig. 1a). This SHF change is due primarily to the sensible and latent heat fluxes (Fig. 1c) that respond to changing air-sea temperature gradients (Frölicher et al. 2015). To the south of the ACC, the atmosphere has warmed more rapidly than the ocean surface such that less heat is lost from the ocean to the atmosphere. In the vicinity of the ACC and north of it, the ocean surface has warmed more rapidly than the atmosphere, with an oceanic heat loss.

Although heat is gained at the southern flank of the ACC (around 60^{o}S), the OHS change peaks at around 45^{o}S (Fig. 2a) and is concentrated in the upper 1000 m (Fig. 2e), which is consistent with previous studies [e.g., Frölicher et al. (2015); Armour et al. (2016)]. The CMIP5 models appear to agree on this aspect as well (Fig. 2c). The mismatch between the location of OHU and OHS can be attributed to the MOC (ψ_{res}) that redistributes heat via OHT divergence/convergence in the Southern Ocean [Frölicher et al. (2015); Armour et al. (2016)]. Moreover, the full MOC in the Southern Ocean undergoes changes in a warming climate. Southern Hemisphere westerly winds strengthen and displace poleward in response to quadrupled CO_2 (Fig. 3a, c), which intensifies and shifts poleward the wind-driven Deacon Cell (Fig. 4a). However, the eddy-induced MOC does not correspondingly intensify to compensate for the variation in the Deacon Cell, but weakens instead (Fig. 4c). This eddy-induced MOC weakening, as will be shown in later sections, is primarily caused by the surface buoyancy flux change due to the direct CO_2 effect rather than the wind change. Over the Southern Ocean, changes in the wind-driven ($\overline{\psi}$) and eddy-induced (ψ^*) MOCs together result in a stronger and poleward shifted residual MOC (ψ_{res}) (Fig. 4e).

To summarize, CMIP5 models show that the Southern Ocean primarily receives heat from atmosphere around 60^{o}S. This incoming heat is redistributed by the residual MOC and mostly stored around 45^{o}S. Various feedbacks, including the wind-induced feedback, play a role in modifying OHU, OHT and thus OHS. In the next section, we will employ an overriding technique to isolate and quantify the effects of these feedbacks.

b. Decomposed response in the CESM overriding experiments

Making use of the overriding experiments (Table 2), we decompose the total climate response in CESM1-CAM5 into the parts due to wind stress change ($Wstr$), surface wind speed change ($Wspd$) and direct CO_2 effect ($dirCO_2$) without any wind changes. The sum of these three parts (denoted as *Sum*) closely replicate the total response (Figs. S1-S3, 8 and 10). Since the wind speed change has an ignorable contribution to SHF and OHT variations (Figs. S1-S3, 8 and 10), we will only focus on the wind stress effect and the direct CO_2 effect in the following.

We start with comparing the wind and direct CO_2 effects on MOC response to quadrupled CO_2. The poleward intensified wind stress shifts the Deacon Cell ($\overline{\psi}$) poleward (in $Wstr$) and strengthens the cell by about 7 Sv (1 Sv = 10^6m^3/s) at its maximum (Fig. 5e). The eddy-driven circulation (ψ^*) is enhanced due to increased isopycnal tilting and baroclinicity (Fig. 6b) and partially offsets the wind-driven Deacon Cell (Fig. 5f). Consequently, the residual MOC (ψ_{res}) generally follows the changes in the Deacon Cell, producing a poleward-intensified circulation (Fig. 5d). On the other hand, the direct CO_2 effect is of the secondary importance in modifying the residual MOC (Fig. 5g). It flattens the isopycnal slope (Fig. 6c) and weakens the eddy-induced component of the MOC (Fig. 5i). However, this reduction in the eddy component is compensated (or over-compensated around 60$^{\text{o}}$S) by an decrease in the mean flow part (Fig. 5h).

Unlike the MOC response, the direct CO_2 effect has a much larger contribution to temperature response than the wind stress. Over the Southern Ocean, the total temperature response shows that the surface layers warm by over 3 K, and the warming decays with depth (Fig. 7a). The strongest penetration of the surface signal into the deeper ocean is around 45$^{\text{o}}$S where the downward Ekman pumping is strongest. The direct CO_2 effect produces a similar warming pattern (Fig. 7c) as the total response (Fig. 7a) and explains most of the warming. The wind stress changes also contribute to a subsurface warming but of a relatively small amplitude. By strengthening and shifting the Deacon Cell and hence the residual MOC poleward, the winds amplify the subsurface warming signal in the region between 40°S and 50°S (with a warming maximum over 1 K) and suppress the signal at higher and lower latitudes (Fig. 7b). This result is consistent with Fyfe et al. (2007).

We further examine the wind and direct CO_2 effects in modifying OHT and its gradient. Consistent with the CMIP5 models (Fig. 8, gray curves), CESM1-CAM5 shows an anomalous equatorward OHT (Fig. 8a, black curve) that peaks around 54°S with OHT divergence and convergence on its poleward and equatorward flanks, respectively (Fig. 10a, skyblue curve). This OHT change is primarily due to the changes in mean flow ($\overline{OHT}$) (Fig. 8b, black curve). The eddy-induced part (OHT^*) partially offsets the mean-flow part to the south of 45°S but strengthens it to the north (Fig. 8c, black curve). Note here, the increased southward eddy heat transport to the south of 45°S does not result from the change of eddy-induced MOC but is mostly accomplished through the advection of temperature anomalies by the climatological eddy-induced MOC. Compared to advective heat transports ($\overline{OHT}$ and OHT^*), the change in diffusive heat transport (OHT^d) is small and localized mostly around 45°S (Fig. 8d, black curve).

Using the overriding technique, we split the total OHT response into the wind-driven and direct CO_2-induced parts. Again, the mean-flow component ($\overline{OHT}$) dominates both parts. Poleward-intensified surface winds generate a dipole-like $\overline{OHT}$ change: an anomalous equatorward (poleward) $\overline{OHT}$ to the south (north) of 45°S (Fig. 8b, blue curve). This wind-driven $\overline{OHT}$ change is primarily accomplished through a MOC change. The shift and strengthening of wind-driven Deacon Cell strengthens the MOC and the associated $\overline{OHT}$ south of 45°S and weakens them to the north (Fig. 8b, blue curve). On the other hand, the direct CO_2 effect causes an anomalous equatorward $\overline{OHT}$ in most regions of the Southern Ocean, with a peak at 43-58°S (Fig. 8b, red curve). Unlike its wind-driven counterpart, the direct CO_2-induced $\overline{OHT}$ change is due to ocean warming (Fig. 7c). To the north of 62^{o}S, most of the CO_2-induced warming concentrates in the upper 1000 m (Fig. 7c) and is carried northward by the upper branch of the climatological mean MOC. Comparing the wind-driven and direct CO_2-induced $\overline{OHT}$ changes, we find that (1) their magnitudes are on the same order (0.1-0.2 PW, 1PW = 10^{15} Watt); and (2) they both transport heat equatorward up to 45^{o}S but work against each other to the north of this latitude (Fig. 8b). These results implicate that the wind and direct CO_2 effects are of equal importance in shaping the OHT response over the Southern Ocean.

Besides the OHT variations, surface wind changes also play a pivotal role in shaping the surface heat fluxes and heat uptake (SHF and OHU) over the Southern Ocean. In response to the poleward-intensified surface winds, ocean gains heat (positive anomalous SHF) around 60^{o}S (Fig. 9c-d), which is primarily related to an OHT divergence induced by enhanced wind-driven MOC (a point to return later). Meanwhile, ocean loses heat (negative anomalous SHF) around 45^{o}S. This is because anomalous upper level convergent and subducting motion there warms the ocean surface and leads to oceanic heat loss via sensible and latent heat fluxes (Fig. 9d, dodger-blue curve).

In contrast, the direct CO_2 effect brings about net heat gain over the Southern Ocean (Fig. 9e-f), with most heat entering the upwelling region (around 60^{o}S) via sensible and latent heat fluxes (Fig. 9f, dodger-blue curve). This is predominantly the result of passive heat uptake by the background mean Southern Ocean circulation, the salient characteristic of which is a monotonic decrease with depth of temperature anomalies below the mixed layer in the open ocean. As the direct CO_2-indcued MOC change is secondary (although the eddy part is still important), we could treat the direct CO_2-induced part as passive uptake [note here that this treatment is only approximately valid in the Southern Ocean, since the increasing CO_2 hardly alters the residual

MOC in the Southern Ocean but can greatly change the MOC in the Atlantic (Liu et al. 2017), also c.f. Marshall et al. (2015) for the rationale of this treatment] and the wind-driven part as active uptake. This is supported by a recent study (Garuba et al. 2018) which showed that passive ocean tracers coupled to the atmosphere under increasing CO_2 can produce almost the same pattern as that of the direct CO_2-induced heat uptake here (Fig. 9e) while active heat uptake derived from tracer experiments is very similar to the wind-driven heat uptake (Fig. 9c). Overall, comparing the wind-driven, the direct CO_2-induced and the total OHU, we find that (1) the wind-driven part accounts for the total heat loss around 45^{o}S, and (2) the wind-driven and direct CO_2-induced parts explain about one third and two thirds of the total heat gain around 60^{o}S, respectively (Fig. 9b, d, and f, black curves).

Based on Eq. (8), we can close the heat budget and quantify the contributions of the wind-driven and direct CO_2-induced feedbacks to Southern Ocean heat uptake and storage. We first focus on the heat budget in the total response where the maximum surface heat gain at around 60^{o}S (Fig. 10a, black curve) is balanced mostly by an anomalous OHT divergence (Fig. 10a, skyblue curve). This result is consistent with (Armour et al. 2016), indicating that the region where most heat enters is not the place where the ocean warms most. Following an anomalous equatorward OHT (Fig. 8a), most of the heat is carried and stored north of 60^{o}S (Fig. 10a, orange-red curve). The maximum of OHS occurs at 45^{o}S at a rate of 0.38 ZJ/year (1ZJ = 10^{21} joules). It is significant that the OHS patterns are similar between CESM1-CAM5 (Fig. 10a, orange-red curve) and the CMIP5 models (Fig. 10a, orange curves), although the OHU and OHT patterns are recognizably different among these models (Fig. 10a).

To further quantify the contributions from the wind-driven and direct CO_2-induced processes, we examine the heat budgets related to both processes. We find that the poleward-shifted and intensified surface winds displace and strengthen the Deacon Cell and residual MOC, thus leading to an *OHT* divergence (convergence) around 60°S (45°S). Meanwhile, the wind-induced feedback brings about a heat gain (loss) at 60°S (45°S) in the surface flux (Fig. 10b). As a result, the wind-driven *OHS* peaks at 46°S at a rate of 0.07 ZJ/year/degree (degree in the unit denotes degree of latitude) and contributes to about one fifth of the total *OHS* maximum (Fig. 10f, blue curve). When we compute the heat budget over the Southern Ocean (from the Antarctic coast to 34°S and from ocean surface to the bottom), we find that the wind-driven *OHU* is -0.9 ZJ/year, which means that the poleward-shifted, intensified winds act to release heat from ocean to atmosphere. At the same time, the wind changes induce an anomalous *OHT* of -1.9 ZJ/year across 34°S by altering the MOC (ψ_{res}). Not only does this anomalous poleward heat transport compensate the wind-induced heat loss at the ocean surface but also results in a net heat storage of 1.0 ZJ/year that accounts for about one eighth of basin-integrated *OHS*.

On the other hand, the direct CO_2-induced warming brings about an anomalous *OHT* divergence and a maximum heat gain at 60°S (Fig. 10d). This combination leads to an *OHS* peaking at 42°S at a rate of 0.30 ZJ/year/degree, which yields about four fifths of the total *OHS* maximum (Fig. 10f, red curve). The basin-integrated heat budget further shows that the direct CO_2 effect induces an *OHU* of 11.0 ZJ/year at the ocean surface and an *OHT* of 4.2 ZJ/year out of the basin across 34°S, leaving a net heat storage of 6.8 ZJ/year that accounts for about seven eighths of basin-integrated *OHS* over the Southern Ocean. It is noteworthy that the peak of the wind-driven *OHS* is located about 4 degrees south of the peak of the direct CO_2-induced *OHS* (Fig. 10f); that is, the poleward-intensified winds act to distribute oceanic heat to a more poleward location in a warming climate.

4. Conclusion and discussions

In this study, we explore the Southern Ocean heat uptake, redistribution and storage in response to quadrupled CO_2. We first identify the general characteristics of climate response from ten CMIP5 climate models, which show that most heat enters the Southern Ocean around 60^{o}S but is stored around 45^{o}S, as consistent with other studies [e.g., Frölicher et al. (2015); Armour et al. (2016)]. This result suggests that heat in the ocean interior is redistributed by the MOC, which in turns, is related to surface wind changes. To isolate and quantify the wind effect, we apply an overriding technique to a climate model, CESM1-CAM5, and decompose the total climate response into the wind-driven and direct CO_2-induced parts. For the wind-driven part, the poleward-intensified surface winds shift and strengthen the Deacon Cell and hence the residual MOC, which generates an anomalous OHT divergence (convergence) at 60^{o}S (45^{o}S). Further, in response to wind-driven circulation change, the Southern Ocean gains heat around 60^{o}S but loses heat around 45^{o}S. As a result, the wind-driven OHS peaks at 46^{o}S at a rate of 0.07 ZJ/year/degree and contributes to about one fifth of the total OHS maximum. On the other hand, the direct CO_2 effect barely modifies the residual MOC but accounts for most temperature variations, leading to anomalous equatorward OHT and heat gain in most regions of the Southern Ocean. The heat gain is maximum at 60^{o}S where the anomalous OHT diverges. As a result, the direct CO_2-induced OHS peaks at 42^{o}S instead of 60^{o}S, at a rate of 0.30 ZJ/year/degree and contributes to four fifths of the total OHS maximum.

Another interesting result of our study is the weakening of the eddy-induced MOC over the Southern Ocean in response to quadrupled CO_2 (Fig. 4c-d). In both CESM1-CAM5 and CMIP5 models, the eddy-induced MOC weakens when Southern Hemisphere westerly winds strengthen and shift poleward. Based on the CESM1-CAM5 overriding experiments, we find that the weakening of the eddy-induced MOC is primarily caused by the direct CO_2 effect. Two processes compete under quadrupled CO_2. On the one hand, the poleward-intensified winds enhance isopyncal tilting (Fig. 6b) and increase the eddy-induced MOC by 1 Sv (Fig. 5f). On the other hand, the direct CO_2-induced buoyancy change suppresses isopyncal tilting (Fig. 6b) and decreases the eddy-induced MOC by 2 Sv (Fig. 5f), which overshadows the former effect, manifesting in a weaker eddy-induced MOC.

Our heat budget analyses on CESM1-CAM5 and CMIP5 models reveal that both mean flow and eddy could be important to Southern Ocean heat uptake and redistribution. Particularly, the peak of the OHT divergence around 60^{o}S is primarily driven by an enhanced mean-flow part rather than a reduced eddy part, which is in agreement with those previous studies identifying this mechanism [Cai et al. (2010); Kuhlbrodt and Gregory (2012); Marshall and Zanna (2014); Bryan et al. (2014); Exarchou et al. (2015)]. On the other hand, both eddy (plus diffusion) and mean-flow parts contribute to an anomalous northward OHT to the north of 45^{o}S and hence an OHT convergence around 45^{o}S. This is consistent with Morrison et al. (2016).

We use a quadrupled CO_2 forcing in this study for purpose of large signal-to-noise ratio and a clean single-factor view of future warming climate. In the real world, many other factors such as ozone variations, can also play a role in Southern Ocean heat uptake and redistribution. As discussed in the introduction part, a large portion of wind change (and hence the wind effect) can be attributed to ozone depletion during recent years. Nevertheless, ozone is predicted to recover in the RCP (Representative Concentration Pathway) scenarios so that the ozone effect will become increasingly weak, which justifies the usage of a single CO_2 increase as a good approximation to future climate forcing. Here, we suspect that some climate response, such as the weakened eddy-induced MOC, may depend on the strength or the form of forcing. In our case, a quadrupled CO_2 is a strong forcing that allows a large buoyancy flux change to overcome the wind effect and dominate in regulating isopyncal tilting and baroclinicity over the Southern Ocean. However, the response of eddy-induced MOC is likely subject to change if under a weaker CO_2 forcing or a combined forcing with ozone change.

We show a well agreement between CESM1-CAM5 and other CMIP5 models in the response of Southern Ocena heat uptake, redistribution and storage under quadrupled CO_2 forcing. This is indeed significant since CMIP5 models are known to have biases in their climatological temperature gradients and background OHC [e.g., Schneider and Deser (2017); Kostov et al. (2017)]. The agreement between CESM1-CAM5 and the other CMIP5 models may be due to the dominant role of the direct CO_2 effect that accounts for 80% of OHS. Any model biases in the climatological temperature gradients would affect only the remaining 20% of OHS due to wind-induced changes.

In this study, we do not discuss the effect of sea ice on Southern Ocean heat uptake and redistribution because this effect is not robust in CESM1-CAM5. Previous studies [e.g. Bitz et al. (2006)] suggest that the sea ice response around Antarctica to increasing CO_2 causes surface freshening and weakened convection, which further reduces the vertical and meridional temperature gradients, leading to a deep warming below 500 m that extends to a several kilometer depth and spread equatorward from the Antarctic sea ice area. This deep-warming pattern is present in some of the CMIP5 models (Fig. 2e) but not in CESM1-CAM5 (Fig. 2f). In CESM1-CAM5, the warming is limited to the upper 1000m close to the coast of Antarctica. Exploring the sea ice effect will be important in our future work.

Acknowledgments. This work was supported by the National Science Foundation (NSF AGS-1249145; NSF OPP-1741841), the DOE Office of Science (DE-SC0016538) and the Office of Science of the U. S. Department of Energy as part of the Regional and Global Climate Modeling

program. The CMIP5 data are publicly available through the portal of the U.S. Earth System Grid Center for Enabling Technologies on the page http://pcmdi9.llnl.gov/.

References

Abernathey, R., J. Marshall, and D. Ferreira, 2011: The dependence of Southern Ocean meridional overturning on wind stress. *J. Phys. Oceanogr.*, **41**, 2261–2278.

Armour, K. C., J. Marshall, J. R. Scott, A. Donohoe, and E. R. Newsom, 2016: Southern Ocean warming delayed by circumpolar upwelling and equatorward transport. *Nature Geosci.*, **9**, 549–554.

Banks, H. T., and J. M. Gregory, 2006: Mechanisms of ocean heat uptake in a coupled climate model and the implications for tracer based predictions of ocean heat uptake. *Geophys. Res. Lett.*, **33**, doi:10.1029/2005GL025352.

Bishop, S. P., P. R. Gent, F. O. Bryan, A. F. Thompson, M. C. Long, and R. Abernathey, 2016: Southern Ocean overturning compensation in an eddy-resolving climate simulation. *J. Phys. Oceanogr.*, **46**, 1575–1592.

Bitz, C. M., P. R. Gent, R. A. Woodgate, M. M. Holland, and R. Lindsay, 2006: The influence of sea ice on ocean heat uptake in response to increasing CO_2. *J. Climate*, **19**, 2437–2450.

Bryan, F. O., P. R. Gent, and R. Tomas, 2014: Can southern ocean eddy effects be parameterized in climate models? *J. Climate*, **27**, 411–425.

Bryan, K., S. Manabe, and M. J. Spelman, 1988: Interhemispheric asymmetry in the transient response of a coupled ocean-atmosphere model to a CO_2 forcing. *J. Phys. Oceanogr.*, **18**, 851–867.

Cai, W., T. Cowan, S. Godfrey, and S. Wijffels, 2010: Simulations of processes associated with the fast warming rate of the southern midlatitude ocean. *J. Climate*, **23**, 197–206.

Chen, X., and K.-K. Tung, 2014: Varying planetary heat sink led to global-warming slowdown and acceleration. *Science*, **345**, 897–903.

Church, J. A., D. Monselesan, J. M. Gregory, and B. Marzeion, 2013: Evaluating the ability of process based models to project sea-level change. *Environ. Res. Lett.*, **8**, 014 051.

Church, J. A., and Coauthors, 2011: Revisiting the earth's sea-level and energy budgets from 1961 to 2008. *Geophys. Res. Lett.*, **38**, doi:10.1029/2011GL048794.

Dalan, F., P. H. Stone, and A. P. Sokolov, 2005: Sensitivity of the ocean's climate to diapycnal diffusivity in an EMIC. Part II: Global warming scenario. *J. Climate*, **18**, 2482–2496.

Döös, K., and D. J. Webb, 1994: The Deacon cell and the other meridional cells of the Southern Ocean. *J. Phys. Oceanogr.*, **24**, 429–442.

Downes, S. M., and A. M. Hogg, 2013: Southern Ocean circulation and eddy compensation in CMIP5 models. *J. Climate*, **26**, 7198–7220.

Durack, P. J., P. J. Gleckler, F. W. Landerer, and K. E. Taylor, 2014: Quantifying underestimates of long-term upper-ocean warming. *Nature Clim. Change*, **4**, 999–1005.

Exarchou, E., T. Kuhlbrodt, J. M. Gregory, and R. S. Smith, 2015: Ocean heat uptake processes: A model intercomparison. *J. Climate*, **28**, 887–908.

Farneti, R., T. L. Delworth, A. J. Rosati, S. M. Griffies, and F. Zeng, 2010: The role of mesoscale eddies in the rectification of the Southern Ocean response to climate change. *J. Phys. Oceanogr.*, **40**, 1539–1557.

Ferreira, D., J. Marshall, C. M. Bitz, S. Solomon, and A. Plumb, 2015: Antarctic Ocean and Sea Ice Response to Ozone Depletion: A Two-Time-Scale Problem. *J. Climate*, **28**, 1206–1226.

Frölicher, T. L., J. L. Sarmiento, D. J. Paynter, J. P. Dunne, J. P. Krasting, and M. Winton, 2015: Dominance of the Southern Ocean in Anthropogenic Carbon and Heat Uptake in CMIP5 Models. *J. Climate*, **28**, 862–886.

Fyfe, J. C., 2006: Southern Ocean warming due to human influence. *Geophys. Res. Lett.*, **33**, doi:10.1029/2006GL027247.

Fyfe, J. C., O. A. Saenko, K. Zickfeld, M. Eby, and A. J. Weaver, 2007: The role of poleward-intensifying winds on Southern Ocean warming. *J. Climate*, **20**, 5391–5400.

Garuba, W., J. Lu, F. Liu, and H. Singh, 2018: The Active Role of the Ocean in the Temporal Evolution of Climate Sensitivity. *Geophys. Res. Lett.*, **45**, 306–315.

Gent, P. R., and G. Danabasoglu, 2011: Response to increasing Southern Hemisphere winds in CCSM4. *J. Climate*, **24**, 4992–4998.

Gent, P. R., and J. C. Mcwilliams, 1990: Isopycnal mixing in ocean circulation models. *J. Phys. Oceanogr.*, **20**, 150–155.

Gille, S. T., 2002: Warming of the Southern Ocean since the 1950s. *Science*, **295**, 1275–1277.

Gillett, N. P., and D. W. J. Thompson, 2003: Simulation of recent Southern Hemisphere climate change. *Science*, **302**, 273–275.

Gregory, J. M., 2000: Vertical heat transports in the ocean and their effect on time-dependent climate change. *Clim. Dyn.*, **16**, 501–515.

Gregory, J. M., and Coauthors, 2001: Comparison of results from several AOGCMs for global and regional sea-level change 1900–2100. *Clim. Dyn.*, **18**, 225–240.

Griffies, S. M., and Coauthors, 2015: Impacts on ocean heat from transient mesoscale eddies in a hierarchy of climate models. *J. Climate*, **28**, 952–977.

Hallberg, R., and A. Gnanadesikan, 2006: The role of eddies in determining the structure and response of the wind-driven southern hemisphere overturning: Results from the Modeling Eddies in the Southern Ocean (MESO) project. *J. Phys. Oceanogr.*, **36**, 2232–2252.

Hieronymus, M., and J. Nycander, 2013: The budgets of heat and salinity in NEMO. *Ocean Modell.*, **67**, 28 – 38.

Hogg, A. M. C., M. P. Meredith, J. R. Blundell, and C. Wilson, 2008: Eddy heat flux in the Southern Ocean: Response to variable wind forcing. *J. Climate*, **21**, 608–620.

Holland, M. M., D. A. Bailey, B. P. Briegleb, B. Light, and E. Hunke, 2012: Improved sea ice shortwave radiation physics in CCSM4: The impact of melt ponds and aerosols on Arctic sea ice. *J. Climate*, **25**, 1413–1430.

Huang, B., P. H. Stone, A. P. Sokolov, and I. V. Kamenkovich, 2003: The deep-ocean heat uptake in transient climate change. *J. Climate*, **16**, 1352–1363.

Hurrell, J. W., and Coauthors, 2013: The community earth system model: A framework for collaborative research. *B. Am. Meteorol. Soc.*, **94**, 1339–1360.

Hwang, Y.-T., S.-P. Xie, C. Deser, and S. M. Kang, 2017: Connecting tropical climate change with southern ocean heat uptake. *Geophys. Res. Lett.*, **44**, 9449–9457, doi:10.1002/2017GL074972.

Kostov, Y., J. Marshall, U. Hausmann, K. C. Armour, D. Ferreira, and M. M. Holland, 2017: Fast and slow responses of Southern Ocean sea surface temperature to SAM in coupled climate models. *Clim. Dyn.*, **48**, 1595–1609.

Kuhlbrodt, T., and J. M. Gregory, 2012: Ocean heat uptake and its consequences for the magnitude of sea level rise and climate change. *Geophys. Res. Lett.*, **39**, L18 608, doi:10.1029/2012GL052952.

Large, W. G., J. C. McWilliams, and S. C. Doney, 1994: Oceanic vertical mixing: A review and a model with a nonlocal boundary layer parameterization. *Rev. Geophys.*, **32**, 363–403.

Lawrence, D. M., K. W. Oleson, M. G. Flanner, C. G. Fletcher, P. J. Lawrence, S. Levis, S. C. Swenson, and G. B. Bonan, 2012: The CCSM4 Land Simulation, 1850–2005: Assessment of Surface Climate and New Capabilities. *J. Climate*, **25**, 2240–2260.

Lin, S.-J., 2004: A "vertically lagrangian" finite-volume dynamical core for global models. *Mon. Wea. Rev.*, **132**, 2293–2307.

Liu, W., J. Lu, and S.-P. Xie, 2015: Understanding the Indian Ocean response to double CO_2 forcing in a coupled model. *Ocean Dyn.*, **65**, 1037–1046.

Liu, W., S.-P. Xie, Z. Liu, and J. Zhu, 2017: Overlooked possibility of a collapsed Atlantic Meridional Overturning Circulation in warming climate. *Sci. Adv.*, **3**, e1601 666, doi:10.1126/sciadv.1601666.

Liu, W., S.-P. Xie, and J. Lu, 2016: Tracking ocean heat uptake during the surface warming hiatus. *Nature Commun.*, **7**, 10 926.

Lu, J., and B. Zhao, 2012: The role of oceanic feedback in the climate response to doubling CO_2. *J. Climate*, **25**, 7544–7563.

Manabe, S., K. Bryan, and M. J. Spelman, 1990: Transient response of a global ocean-atmosphere model to a doubling of atmospheric carbon dioxide. *J. Phys. Oceanogr.*, **20**, 722–749.

Manabe, S., R. J. Stouffer, M. J. Spelman, and K. Bryan, 1991: Transient responses of a coupled ocean-atmosphere model to gradual changes of atmospheric CO_2. Part I. Annual mean response. *J. Climate*, **4**, 785–818.

Marshall, D. P., and L. Zanna, 2014: A conceptual model of ocean heat uptake under climate change. *J. Climate*, **27**, 8444–8465.

Marshall, J., and T. Radko, 2003: Residual-mean solutions for the Antarctic Circumpolar Current and its associated overturning circulation. *J. Phys. Oceanogr.*, **33**, 2341–2354.

Marshall, J., J. R. Scott, K. C. Armour, J.-M. Campin, M. Kelley, and A. Romanou, 2015: The ocean's role in the transient response of climate to abrupt greenhouse gas forcing. *Clim. Dyn.*, **44**, 2287–2299.

Morrison, A. K., S. M. Griffies, M. Winton, W. G. Anderson, and J. L. Sarmiento, 2016: Mechanisms of Southern Ocean heat uptake and transport in a global eddying climate model. *J. Climate*, **29**, 2059–2075.

Morrison, A. K., O. A. Saenko, A. M. Hogg, and P. Spence, 2013: The role of vertical eddy flux in Southern Ocean heat uptake. *Geophys. Res. Lett.*, **40**, 5445–5450.

Neale, R. B., and coauthors, 2012: Description of the NCAR Community Atmosphere Model (CAM 5.0). NCAR Tech. Note NCAR/TN-486, NCAR, 264 pp.

Oke, P. R., and M. H. England, 2004: Oceanic response to changes in the latitude of the Southern Hemisphere subpolar westerly winds. *J. Climate*, **17**, 1040–1054.

Purkey, S. G., and G. C. Johnson, 2010: Warming of global abyssal and deep Southern Ocean waters between the 1990s and 2000s: Contributions to global heat and sea level rise budgets. *J. Climate*, **23**, 6336–6351.

Roemmich, D., J. Church, J. Gilson, D. Monselesan, P. Sutton, and S. Wijffels, 2015: Unabated planetary warming and its ocean structure since 2006. *Nature Clim. Change*, **5**, 240–245.

Rose, B. E. J., K. C. Armour, D. S. Battisti, N. Feldl, and D. D. B. Koll, 2014: The dependence of transient climate sensitivity and radiative feedbacks on the spatial pattern of ocean heat uptake. *Geophys. Res. Lett.*, **41**, 1071–1078.

Schneider, D. P., and C. Deser, 2017: Tropically driven and externally forced patterns of Antarctic sea ice change: reconciling observed and modeled trends. *Clim. Dyn.*, doi:10.1007/s00382-017-3893-5.

Sen Gupta, A., and M. H. England, 2006: Coupled Ocean–Atmosphere–Ice Response to Variations in the Southern Annular Mode. *J. Climate*, **19**, 4457–4486.

Sen Gupta, A., A. Santoso, A. S. Taschetto, C. C. Ummenhofer, J. Trevena, and M. H. England, 2009: Projected changes to the Southern Hemisphere ocean and sea ice in the IPCC AR4 climate models. *J. Climate*, **22**, 3047–3078.

Smith, R. D., and coauthors, 2010: The Parallel Ocean Program (POP) reference manual. Los Alamos National Laboratory Tech. Rep. LAUR-10-01853, LANL, 140 pp.

Spence, P., J. C. Fyfe, A. Montenegro, and A. J. Weaver, 2010: Southern Ocean response to strengthening winds in an eddy-permitting global climate model. *J. Climate*, **23**, 5332–5343.

Swart, N. C., and J. C. Fyfe, 2012: Observed and simulated changes in the southern hemisphere surface westerly wind-stress. *Geophys. Res. Lett.*, **39**, L16 711, doi:10.1029/2012GL052810.

Taylor, K. E., R. J. Stouffer, and G. A. Meehl, 2012: An overview of CMIP5 and the experiment design. *B. Am. Meteorol. Soc.*, **93**, 485–498.

Thompson, D. W. J., and S. Solomon, 2002: Interpretation of recent Southern Hemisphere climate change. *Science*, **296**, 895–899.

van der Veen, C. J., 1988: Projecting future sea level. *Sury. Geophys.*, **9**, 389–418.

Winton, M., S. M. Griffies, B. L. Samuels, J. L. Sarmiento, and T. L. Frölicher, 2013: Connecting changing ocean circulation with changing climate. *J. Climate*, **26**, 2268–2278.

Winton, M., K. Takahashi, and I. M. Held, 2010: Importance of ocean heat uptake efficacy to transient climate change. *J. Climate*, **23**, 2333–2344.

Wolfe, C. L., and P. Cessi, 2010: What sets the strength of the middepth stratification and overturning circulation in eddying ocean models? *J. Phys. Oceanogr.*, **40**, 1520–1538.

Xie, P., and G. K. Vallis, 2012: The passive and active nature of ocean heat uptake in idealized climate change experiments. *Clim. Dyn.*, **38**, 667–684.

LIST OF TABLES

TABLE 1. Ten CMIP5 climate models and their variables used in this study. BSF denotes barotropic streamfunction, SHF denotes net surface heat flux and T denotes ocean temperature. Meridional overturning circulation (MOC) and meridonal ocean heat transport (OHT) include components induced by Eulerian-mean flow, eddies and other processes while all these components are only available in ACCESS1-0, ACCESS1-3 and CCSM4, we thus only include the MOC and OHT from above three models in the analysis. Surface winds denote winds at 10 m above sea surface. Wind velocities (in vector), i.e., (U,V) and wind speed ($Wspd$) is available in nine models (except CCSM4).

Model	BSF	SHF	T	MOC	OHT	(U,V)	$Wspd$
ACCESS1-0	√	√	√	√	√	√	√
ACCESS1-3	√	√	√	√	√	√	√
bcc-csm1-1	√	√	√			√	√
CCSM4	√	√	√	√	√		
GISS-E2-R	√	√	√			√	√
HadGEM2-ES	√	√	√			√	√
IPSL-CM5A-LR	√	√	√			√	√
IPSL-CM5A-MR	√	√	√			√	√
MRI-CGCM3	√	√	√			√	√
NorESM1-M	√	√	√			√	√

TABLE 2. Design of the CESM1-CAM5 overriding experiments. Two baseline runs are preindustrial control ($CTRL$) and abruptly quadrupled CO_2 ($4 \times CO_2$). Based on these two runs, five overriding experiments are conducted to isolate and quantify the wind effect and the direct CO_2 effect. The overriding variables from $CTRL$ and $4 \times CO_2$ are first output for overriding purpose at the frequency of air-sea coupling and will be referred to respectively as $var1x$ and $var4x$, in which var is the overriding variables: wind stress (τ), wind speed (w) and CO_2 (c). To eliminate the climate drift due to overriding, one-year shift is applied to the prescribed overriding variables. The differences between individual pairs of overriding experiments reveal the contributions due to wind stress changes, wind speed changes and the direct CO_2 effect. The total climate response ($4 \times CO_2$ minus $CTRL$) can be replicated by the sum of three contributions.

Experiment	*Wind stress* τ $(1yr\ shift)$	*Wind speed* w $(1yr\ shift)$	CO_2 c	*Purpose*
1. $CTRL$	$1 \times (no)$	$1 \times (no)$	$1\times$	*Baseline*
2. $\tau_1 w_1 c_1$	$1 \times (yes)$	$1 \times (yes)$	$1\times$	*direct CO_2 effect*
3. $\tau_1 w_1 c_4$	$1 \times (yes)$	$1 \times (yes)$	$4\times$	*direct CO_2 effect* $(dirCO_2)$ $(Exp3 - Exp2)$
4. $\tau_4 w_1 c_4$	$4 \times (yes)$	$1 \times (yes)$	$4\times$	*Wind stress effect* $(Wstr)$ $(Exp4 - Exp3)$
5. $\tau_1 w_4 c_4$	$1 \times (yes)$	$4 \times (yes)$	$4\times$	*Wind speed effect* $(Wspd)$ $(Exp5 - Exp3)$
6. $\tau_4 w_4 c_4$	$4 \times (yes)$	$4 \times (yes)$	$4\times$	*Replication* (Sum) $(Exp6 - Exp2)$ *vs* $(Exp7 - Exp1)$
7. $4 \times CO_2$	$4 \times (no)$	$4 \times (no)$	$4\times$	*Baseline*

LIST OF FIGURES

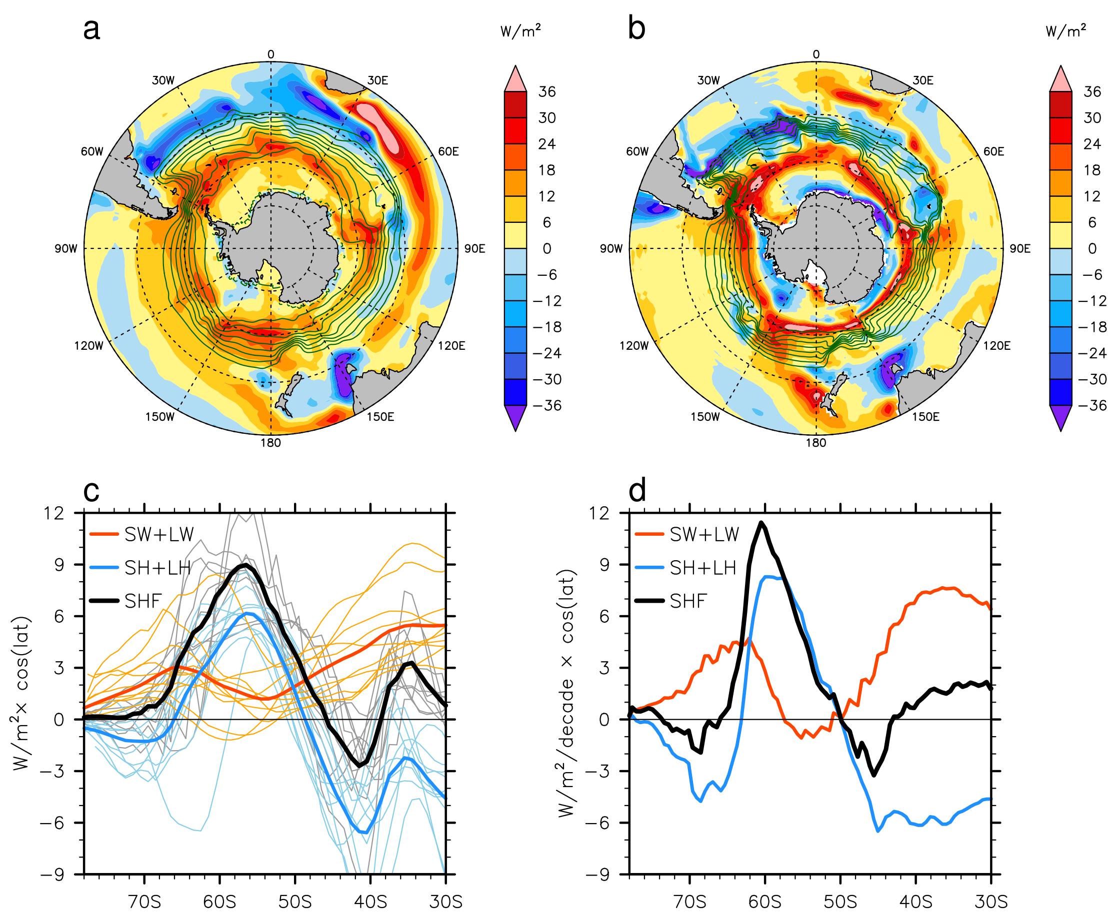

FIG. 1. Changes of net surface heat flux (*SHF*) over the Southern Ocean in response to quadrupled CO_2 (relative to pre-industrial control) for (a) CMIP5 model ensemble mean and (b) CESM1-CAM5, with the path of the Antarctic Circumpolar Current (ACC) superposed that is represented by the contours (green) of barotropic streamfunction (BSF) from CMIP5 model ensemble mean (in panel a) and CESM1-CAM5 (in panel b). Zonal mean changes (weighted by cosine latitude) of *SHF* (black) and its radiative (shortwave and longwave, $SW + LW$, orange-red) and turbulent (sensible and latent, $SH + LH$, dodger-blue) flux components for (c) CMIP5 model ensemble mean and (d) CESM1-CAM5. Results of individual CMIP5 models are also included in panel (c), which is colored gray for *SHF*, orange for $SW + LW$ and light blue for $SH + LH$.

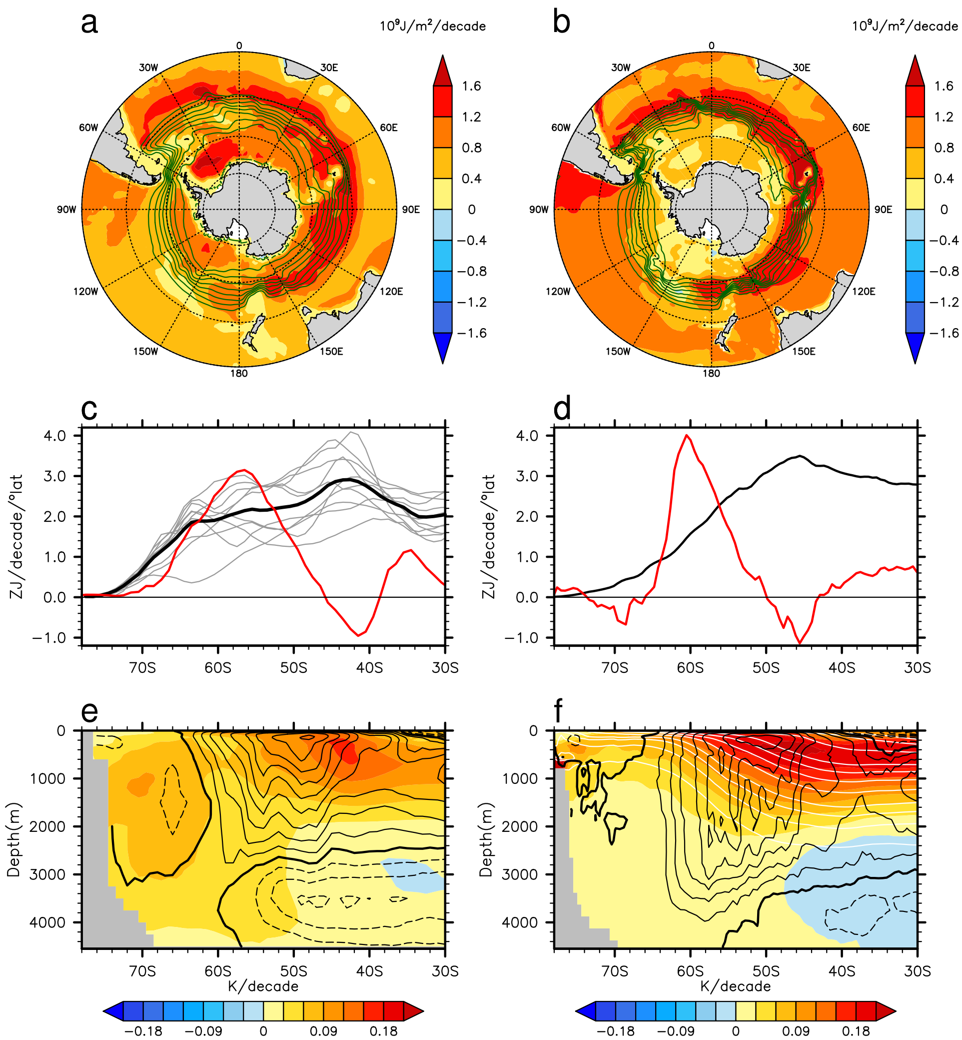

FIG. 2. Trend differences of full-depth integrated ocean heat content (OHC) over the Southern Ocean in response to quadrupled CO_2 (Year 41-90 trend in quadrupled CO_2 minus 50-year trend in pre-industrial control) for (a) CMIP5 model ensemble mean and (b) CESM1-CAM5, with their zonal integrals (black) in panels (c) and (d). The ACC path (denoted by BSF contours, green) is included in panels (a) and (b), and changes of zonal integrals of *SHF* (scaled by 1/4, red) are included in panels (c) and (d). Also, individual CMIP5 model results (gray) are included in panel (c). Trend differences of zonal mean temperature trend over the Southern Ocean in response to quadrupled CO_2 for (e) CMIP5 model ensemble mean and (f) CESM1-CAM5. The preindustrial annual mean (black contours, contouring scheme follows Fig. 4e) meridional overturning circulation (MOC) is included in panels (e) and (f). The preindustrial potential density referenced to the surface σ_0 (white contours, contouring scheme follows Fig. 6a) is included in panel (f).

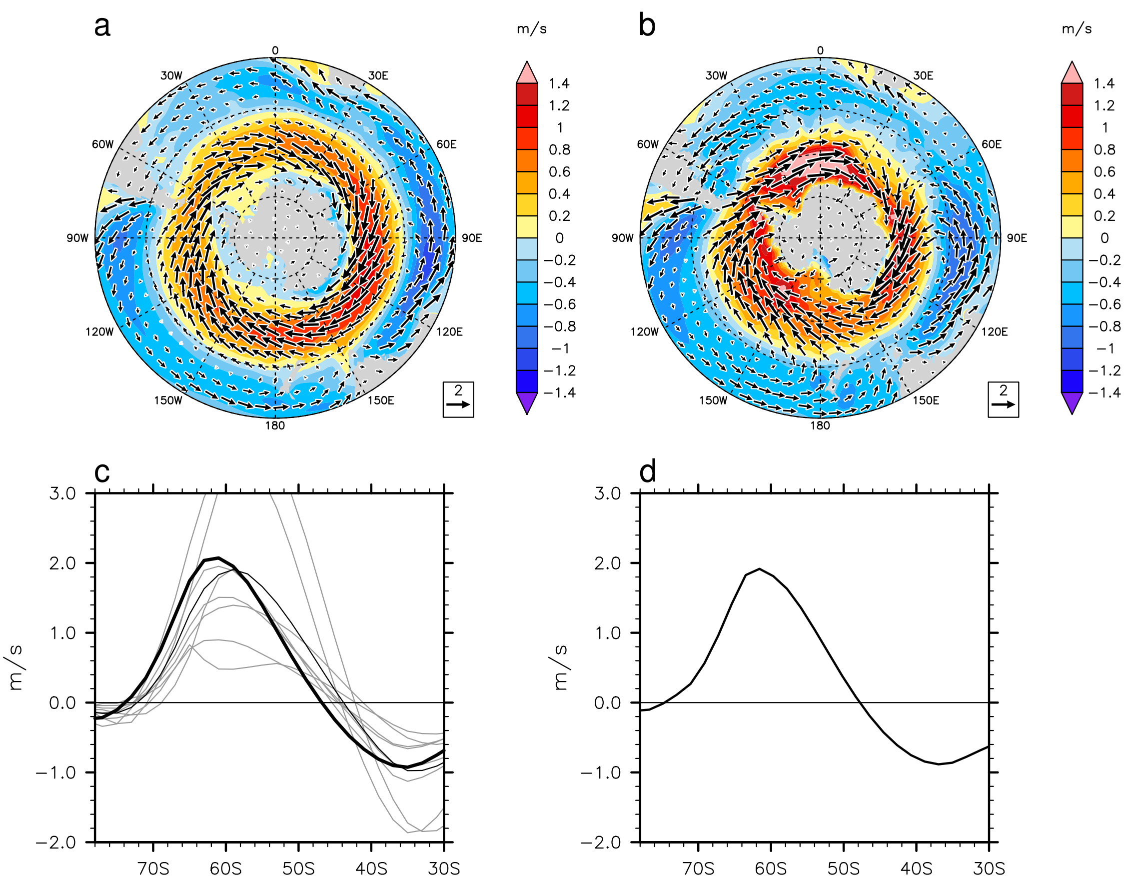

FIG. 3. Changes of annual mean surface winds (vector) and wind speed (shading) over the Southern Ocean in response to quadrupled CO_2 for (a) CMIP5 model ensemble mean and (b) CESM1-CAM5. Zonal mean profiles of zonal wind change (black) for (c) CMIP5 model ensemble mean and (d) CESM1-CAM5. In panel (b), the surface winds of CESM1-CAM5 are taken from the bottom level of CAM5 (993 hpa). In panel (c), individual CMIP5 model results (gray) are included.

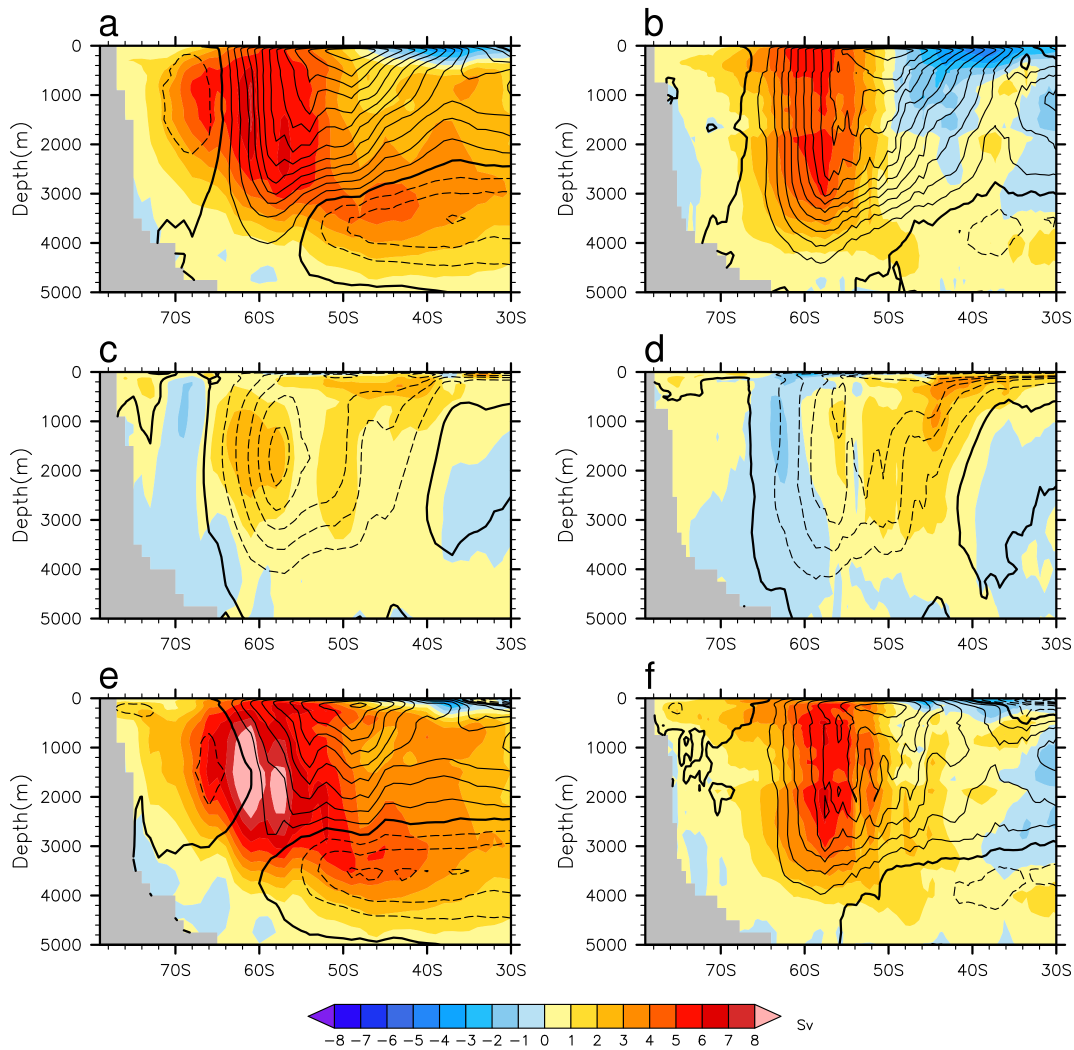

FIG. 4. (left panel) Changes (shading) and preindustrial annual mean (contour) of (a) Eulerian-mean MOC, (c) eddy-induced MOC and (e) residual MOC in response to quadrupled CO_2 for CMIP5 model ensemble mean. (right panel) Same as the left panel but for CESM1-CAM5. The contour interval is 3 Sv, with zero contours thickened and solid (dash) pattern for positive (negative) contours.

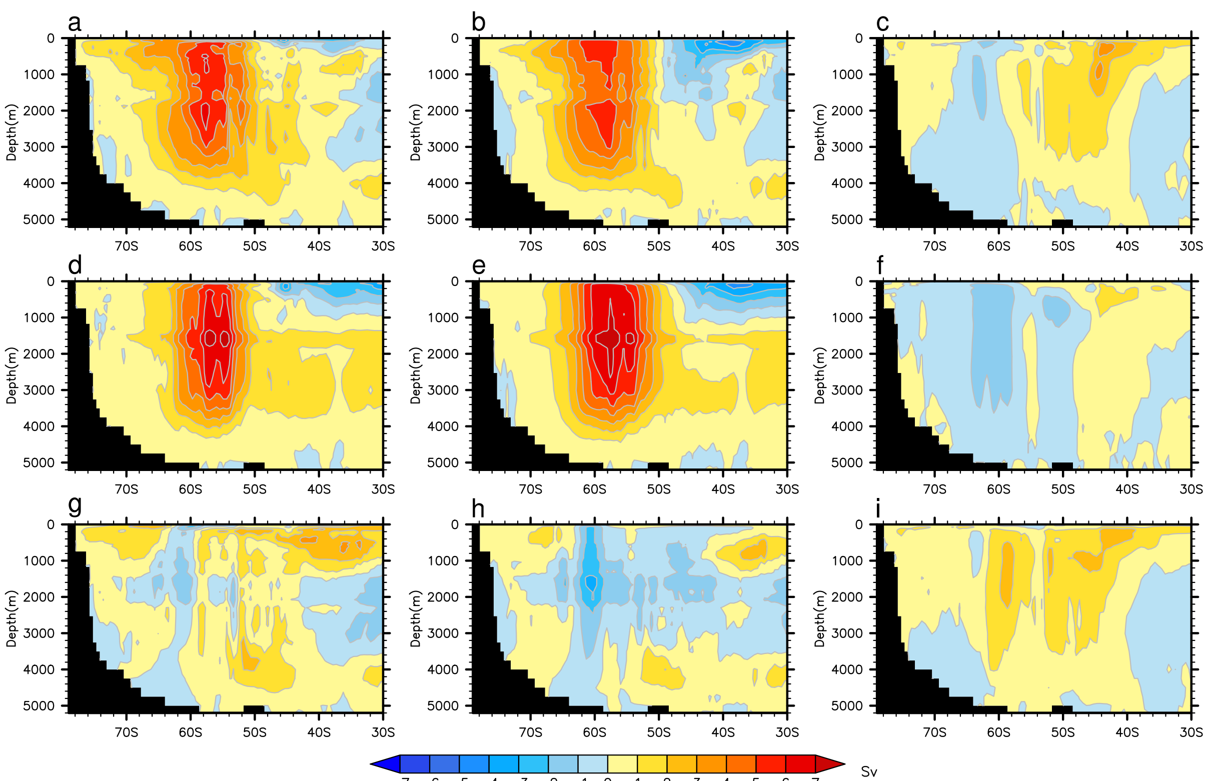

FIG. 5. (top panel) The total response of (a) residual, (b) Eulerian-mean and (c) eddy-induced MOCs in CESM1-CAM5. (mid panel) Same as the top panel but for $Wstr$, the contribution due to wind stress effect. (bottom panel) Same as the top panel but for $dirCO_2$, the contribution due to direct CO_2 effect.

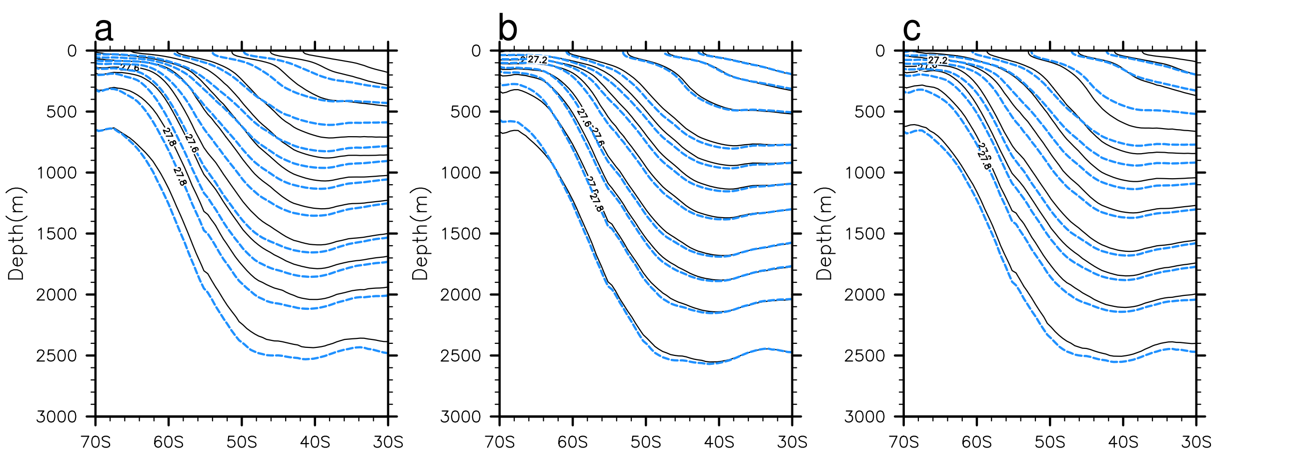

FIG. 6. Zonal mean potential density referenced to the surface σ_0 $\left(kg/m^3\right)$ south of 30^{o}S over the upper 3000 m: (a) $CTRL$ (black, solid) and $4 \times CO_2$ (dodger-blue, dashed); (b) wind stress overriding experiments: $\tau 4w1c4$ (black, solid) and $\tau 1w1c4$ (dodger-blue, dashed), (c) direct $\mathrm{CO_2}$ experiments: $\tau 1w1c1$ (black, solid) and $\tau 1w1c4$ (dodger-blue, dashed) for CESM1-CAM5.

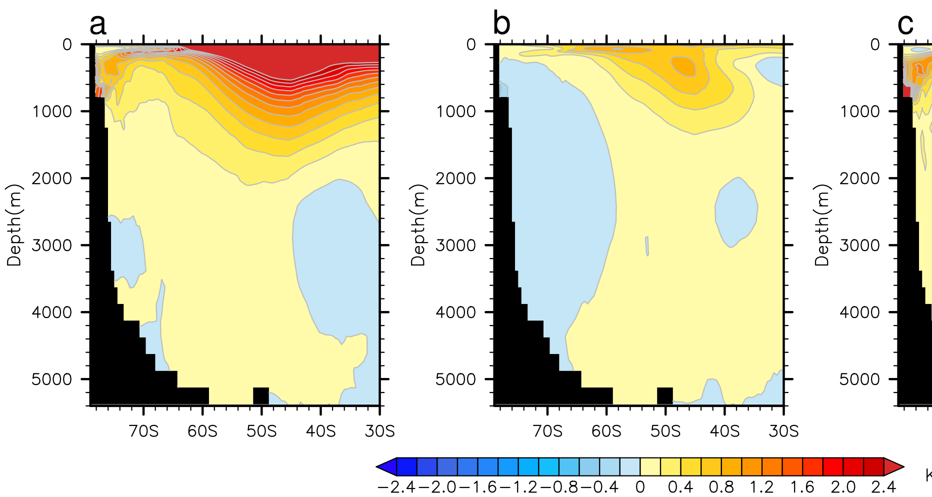

735 FIG. 7. Zonal mean temperature change south of 30°S in (a) the total response, (b) $Wstr$ (the contribution due
736 to wind stress effect) and (c) $dirCO_2$ (the contribution due to direct CO_2 effect) for CESM1-CAM5.

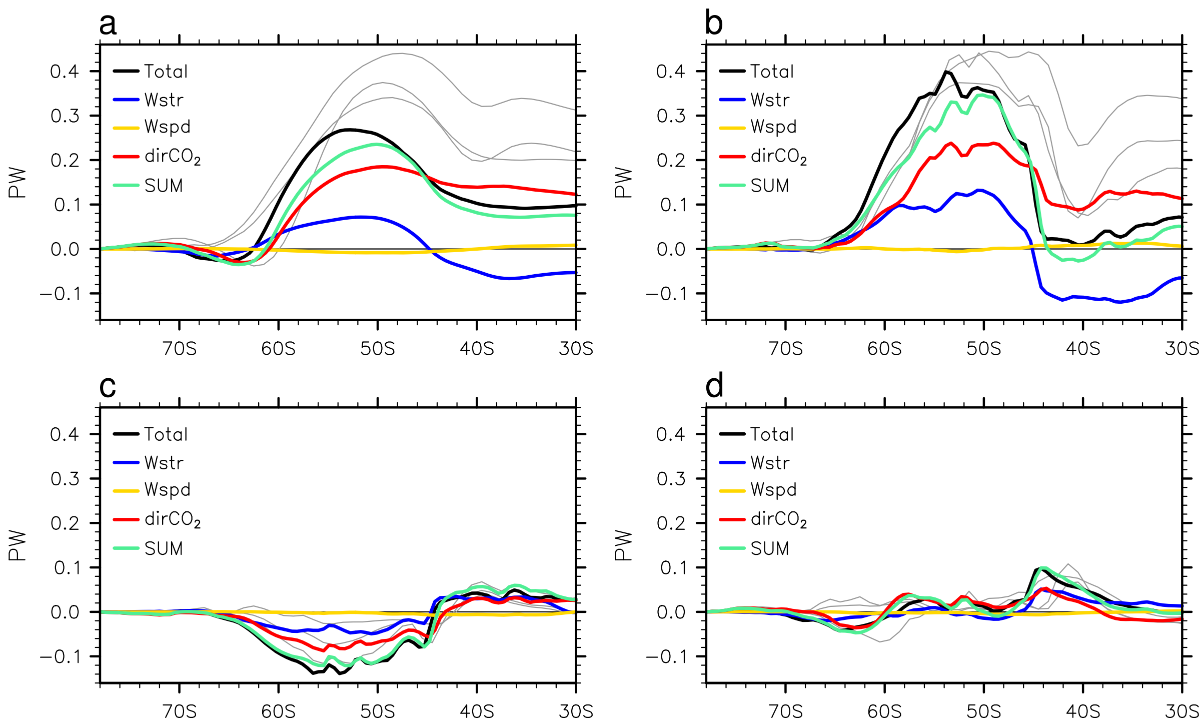

FIG. 8. Changes of (a) meridional ocean heat transport (*OHT*) and its (b) Euler-mean and (c) eddy-induced and (d) diffusive components in the total response (black), the contributions due to wind stress, wind speed and direct CO_2 effects (*Wstr*, blue; *Wspd*, yellow; *dirCO*$_2$, red), and the sum of three contributions (*Sum*, light green) for CESM1-CAM5. The total responses (gray) for CMIP5 models are also included in each panel.

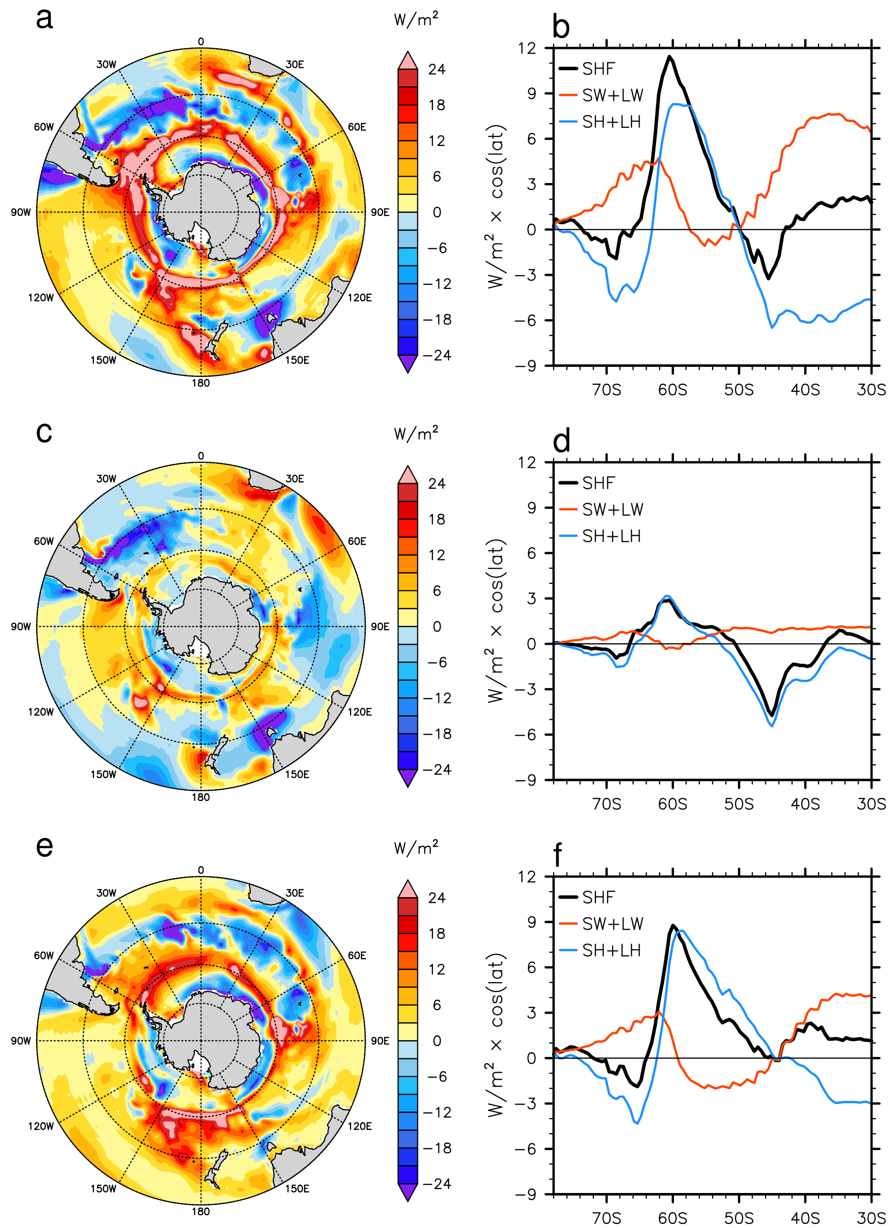

FIG. 9. (left panel) *SHF* change over the Southern Ocean in (a) the total response, (c) *Wstr* (the contribution due to wind stress effect) and (e) *dirCO*$_2$ (the contribution due to direct CO_2 effect) for CESM1-CAM5. (right panel) Zonal mean changes of *SHF* (black), $SW+LW$ (orange-red) and $SH+LH$ (dodger-blue) in the (b) total (d) wind stress and (f) direct CO_2 responses for CESM1-CAM5.

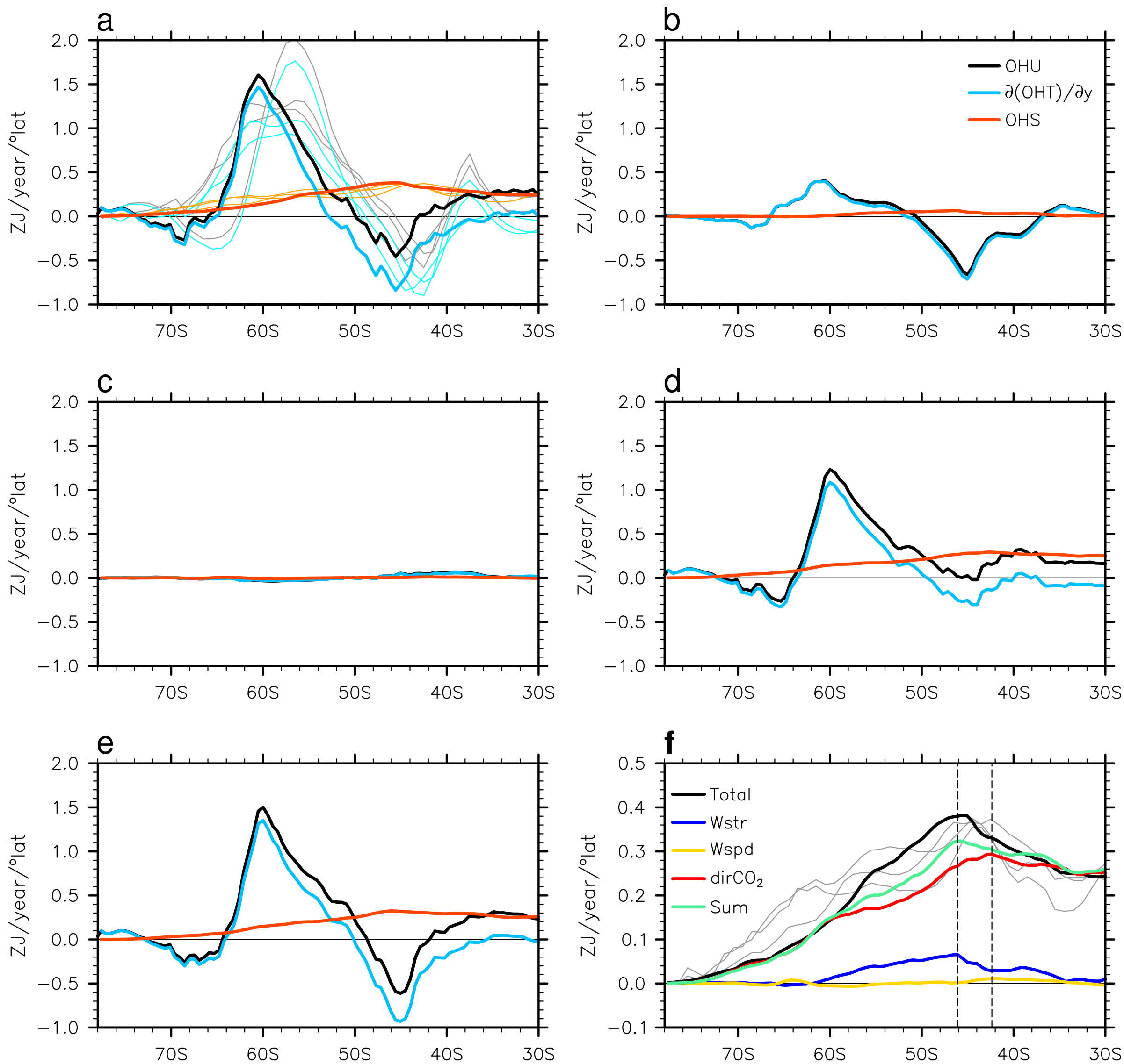

FIG. 10. Heat budget (Eq. 6): OHU (black), $\partial\left(OHT\right)/\partial y$ (skyblue) and OHS (orange-red) south of 30°S in (a) the total response, the contributions due to (b) wind stress, (c) wind speed and (d) direct CO_2 effects, and (e) the sum of three contributions for replication of the total response in CESM1-CAM5. Results from three individual CMIP5 models (OHU, gray; $\partial\left(OHT\right)/\partial y$, cyan; OHS, orange) are also presented in panel (a) as thin curves. OHS is replotted in panel (f) for the comparison of the total response (black), the contributions due to wind stress (blue), wind speed (yellow) and direct CO_2 (red) effects, and the sum of three contributions (light green) for CESM1-CAM5 as well as the total response (gray) for CMIP5 models.